

## Fatigue strength prediction through defects-based analysis of L-PBF 17-4 PH stainless steel

Indrajit Nandi<sup>1,2</sup>, Jade Welsh<sup>3</sup>, Jutima Simsiriwong<sup>\*1,3</sup>, Shuai Shao<sup>1,2</sup>, Nima Shamsaei<sup>1,2</sup>

<sup>1</sup> National Center for Additive Manufacturing Excellence (NCAME), Auburn University,  
Auburn, AL 36849, USA

<sup>2</sup> Department of Mechanical Engineering, Auburn University, Auburn, AL 36849, USA

<sup>3</sup> School of Engineering, University of North Florida, Jacksonville, FL 32224, USA

\*Corresponding author:

Email: j.simsiriwong@unf.edu

Phone: (904) 620-5351

### **Abstract**

Murakami's approach has been used in the high cycle fatigue regime to relate the fatigue limit to the critical defect size and location in additively manufactured (AM) metallic materials. However, the applicability of this model has not yet been thoroughly examined for AM materials in the very high cycle fatigue (VHCF) regime. Therefore, this study investigates the possibility of relating the volumetric defect features to the fatigue strength of 17-4 precipitation hardened (PH) stainless steel (SS) manufactured via laser-powder bed fusion (L-PBF) additive manufacturing technology. The 17-4 PH SS specimens are manufactured using an EOS M290 L-PBF system, heat-treated, machined, polished, and tested in the VHCF regime using an ultrasonic fatigue testing system. Careful fractography has also been performed on all fractured specimens to determine the volumetric defects responsible for the crack initiation.

**Keywords:** Murakami's model; Laser powder bed fusion; Very high cycle fatigue; 17-4 precipitation hardened stainless steel

### **Introduction**

Additive manufacturing (AM) processes for metallic materials, such as laser-powder bed fusion (L-PBF), are becoming more widely used for part fabrication across various industry sectors [1]. This is due to many advantages, particularly its ability to fabricate parts with intricate geometries and net-shaped conditions that cannot be achieved with conventional manufacturing techniques. For AM parts to be fully adopted in safety-critical applications, it is essential to understand the mechanical behavior of AM parts, especially under cyclic loading, to obtain the basis of design allowable for a given application. The fatigue behavior of AM parts is known to be significantly influenced by the formed microstructure and AM process-induced defects [2,3]. Defect's shape, size, and locations affect the stress intensity factor (SIF) surrounding the defects and microstructure, which influences the crack initiation behavior during fatigue loading [4].

In some applications, stainless steel (SS) AM parts, such as those in gas turbines and engines, are subjected to cyclic loading at a very high frequency. The expected service life of these parts can surpass ten million cycles ( $\sim N_f > 10^7$ ) into the very high cycle fatigue (VHCF) regime. In the VHCF regime, where the crack initiation stage is significantly dominant relative to the crack

growth stage, the fatigue resistance of AM parts with the machined surface finish is primarily controlled by the process-induced internal defects [5]. By utilizing the defects characteristics (i.e., defects location and size), a fracture mechanics-based defect-sensitive  $\sqrt{area}$  model, proposed by Murakami [6] has been widely employed to predict the fatigue limit of AM parts, especially in the high cycle fatigue (HCF) regime [7–9]. However, the applicability of this model has not yet been fully examined for AM materials in the VHCF regime.

17-4 precipitation hardened (PH) stainless steel (SS) is a widely used martensitic/austenitic grade SS due to its excellent combination of corrosion resistance, high strength, and tensile toughness, depending on the post-processing heat treatments, making it a suitable material to adopt for the AM processes to fabricate intricate parts [10]. However, the fatigue behavior of 17-4 PH SS is known to be more sensitive to defects, such as pores or inclusions, compared to other metals available for AM [11]. For wrought 17-4 PH SS, fatigue crack initiation in the VHCF regime is typically observed at nonmetallic inclusions or defects [8,12,13]. Nie and Mutoh [13] used the model developed by El Haddad et al. [14] to predict the fatigue limit of 17-4 PH SS by assuming the failure initiates from the material matrix. Schönbauer et al. [15] utilized Murakami's approach to determining the fatigue limit for wrought 17-4 PH SS with varying stress ratios and defect sizes in the VHCF regime, and conservative predictions were obtained. They attributed subsurface inclusion ( $Al_2O_3$ ) as the fatigue crack initiator at lower stress levels, whereas crack initiated at the surface at higher stress levels.

In this study, the applicability of Murakami's model for fatigue strength prediction, for cycles to failure ( $\sim N_f > 10^7$ ), in the VHCF regime for L-PBF 17-4 PH SS has been investigated. Ultrasonic fatigue tests were performed on heat-treated L-PBF 17-4 PH SS specimens fabricated using  $N_2$  as a shielding gas. Fracture surfaces were carefully analyzed to obtain the crack initiation mechanisms in all specimens. The defect characteristics, including the type, location, and size, were analyzed and utilized in the Murakami's model. Finally, the fatigue strength prediction of L-PBF 17-4 PH SS specimens in the VHCF regime were presented and discussed.

## **Materials and Methods**

### **Specimen Fabrication**

Cylindrical 17-4 PH SS bars specimens were fabricated using EOS M290, an L-PBF system, with Ar-atomized 17-4 PH SS powder and  $N_2$  as a shielding gas. The EOS recommended process parameters for 17-4 PH SS were utilized in this study and listed in Table 1. These cylindrical specimens with a height of 75mm and a diameter of 12 mm were fabricated in the vertical direction (z-direction), as shown in Figure 1(a).

Table 1. L-PBF process parameters for 17-4 PH SS used in this study

<b>Power (W)</b>	<b>Scan Speed (mm/s)</b>	<b>Hatching Distance (<math>\mu m</math>)</b>	<b>Layer Thickness (<math>\mu m</math>)</b>
220	755	100	40

Following the fabrication, all specimens were heat-treated according to ASTM A693 standard [16] to CA-H1025 condition, which consists of Condition A (CA) (1050°C/0.5 hour/air-cooled) with one step aging H1025 (552 °C/4 hours/air-cooled), as illustrated in Figure 1(b). After the heat treatment, the cylindrical specimens were machined into final geometries for ultrasonic fatigue testing, as shown in Figure 1(c). All L-PBF 17-4 PH SS specimens were manually polished using 280 grit, 500 grit, 1000 grit, 2000 grit, and 4000 grit silicon carbide papers and cleansed to remove the machining marks from gage section prior to the mechanical testing.

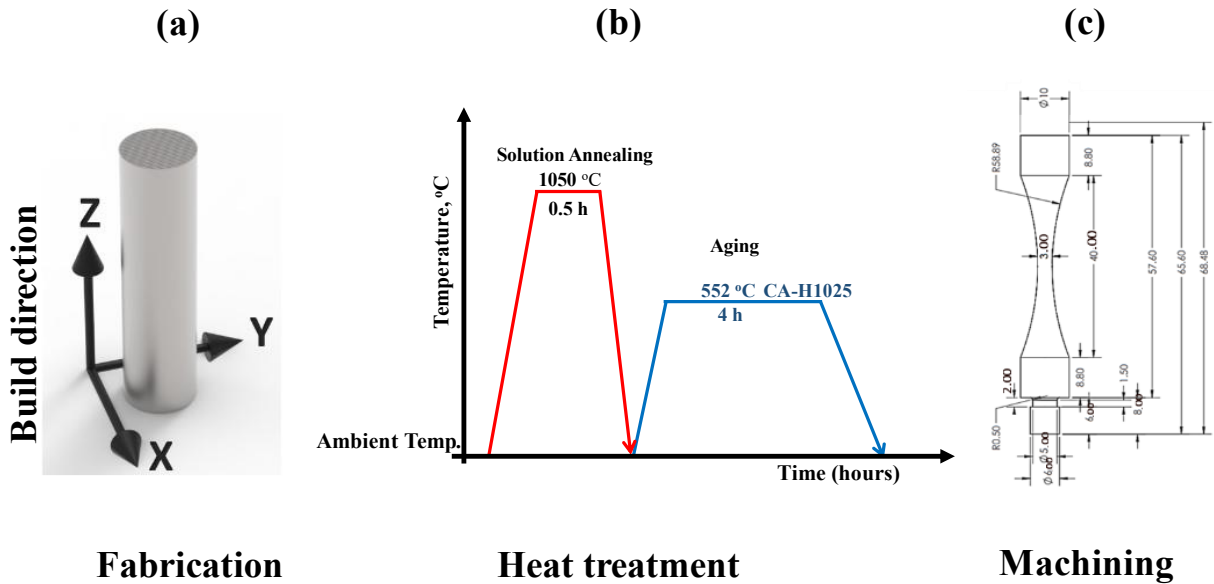


Figure 1. (a) Build direction of the cylindrical specimen, (b) applied heat treatment processes, and (c) final machined geometry of the ultrasonic specimen. All the dimensions are in mm.

### Fatigue testing

Ultrasonic fatigue tests were performed using a Shimadzu USF-2000A ultrasonic fatigue testing machine with uniaxial fully-reversed ( $R = -1$ ) loading condition at a 20 kHz test frequency [17]. Internal heat generation in the specimen due to very high frequency loading was minimized by using an intermittent pulse/pause time of 110 msec and 800 msec oscillations and compressed cooled air. Specimen failures were defined when the resonance frequency of the specimen changed by  $\pm 500$  Hz. Run-out specimens were specified for specimens with no failure after  $10^9$  cycles. All tests were performed at room temperature and relative humidity. Following the ultrasonic fatigue test, fractography analysis was performed for all L-PBF 17-4 PH SS specimens using a Tescan VEGA3 scanning electron microscope (SEM) to investigate the fracture mechanism and crack initiation sites. Before imaging, all the fracture surfaces were cleansed with methanol to remove dirt in a sonication bath.

### Defect-based modeling for fatigue strength prediction

The local stress field around the defects plays a crucial role in fatigue crack initiation and propagation. According to Murakami and Endo [18], the fatigue limit of a material can be

determined based on the threshold stress for a small crack around the defect. The maximum SIF,  $K_{max}$ , of the crack around the defects for an applied uniaxial tensile stress,  $\sigma$ , can be expressed as

$$K_{max} = C\sigma\sqrt{\pi\sqrt{area}} \quad (1)$$

where the parameter  $C$  is 0.5 and 0.65 for surface defects and subsurface/internal defects, respectively. Since defects are usually irregularly shaped, a representative dimension of the crack or  $\sqrt{area}$  is used in this model, which is the area projection of the defects onto the plane perpendicular to the applied stress direction, as illustrated in Table 2. Moreover, the threshold condition for non-propagating cracks can be expressed as follows [19]:

$$\Delta K_{th} = C_1(C_2 + HV)(\sqrt{area})^{1/3} \quad (2)$$

where  $C_1$  and  $C_2$  are material constants, and  $HV$  is the Vickers hardness in  $\text{kgf/mm}^2$ .

At the fatigue limit, when cracks propagating from a defect cease, the SIF range at the crack tip can be expressed as the threshold SIF range ( $\Delta K = \Delta K_{th}$ ). As a result, the fatigue limit,  $\sigma_w$ , of a material can be obtained using the following equation [20].

$$\sigma_w = \frac{m(HV + 120)}{(\sqrt{area})^{1/6}} \quad (3)$$





where the constant  $m$  are 1.41, 1.43, and 1.56 for subsurface defect, surface defect, and internal defect, respectively, as displayed in Table 2. Following Nezhadfar et al. [21] study, subsurface defects are defined by the defects with a linear distance less than 40  $\mu\text{m}$  from the closest surface, while internal defects are those located greater than 40  $\mu\text{m}$  from the surface.

It should be noted that the number of cycles to failure representing the fatigue limit is not specified in Eq. (3). For materials that do not exhibit a fatigue limit, the fatigue strength for a specific number of cycles should be reported, rather than the fatigue limit. Therefore, Wang et al. [21] proposed the modification of Eq. (3) to obtain the fatigue strength for steels by replacing the constant  $m$  with a constant  $\beta$  as:

$$\sigma_w = \frac{\beta(HV + 120)}{(\sqrt{area})^{1/6}} \quad (4)$$

where the parameter  $\beta$  is expressed as  $\beta = 3.09 - 0.12\log(N_f)$  for internal defects and  $\beta = 2.79 - 0.108\log(N_f)$  for surface defects.

Table 2. Location of a defect in a specimen and  $\sqrt{area}$  calculation [9].

Defect Location	(a) Surface	(b) Subsurface	(c) Internal	$\sqrt{area}$ calculation
Pattern				
$m$	1.43	1.41	1.56	

### Results and discussions

The stress-life (S-N) results from the ultrasonic fatigue testing are shown in Figure 2. The results indicate that the fatigue life of L-PBF 17-4 PH SS ultrasonic specimens spans from low cycle to beyond  $10^7$  reversals to failure, i.e., into the VHCF regime, and the horizontal asymptote of the S-N curve to determine the classical fatigue limit is not observed. It should be noted that the detailed microstructure analysis as well as the statistical distribution of defects obtained via x-ray CT scan of these specimens are not in the scope of the current work and can be found in a different study [22]. Also, in Figure 2, the origin of fatigue cracks (i.e., surface/subsurface defect or internal defect) was also identified. The fatigue failure was observed to originate from defects in different regions, similar to other VHCF studies for wrought high-strength steels [23]. As seen in Figure 2, as stress amplitude decreases, fatigue life increases into the VHCF regime where crack initiation transitions from surface/subsurface to the internal region of the specimen, which approximately occurs at  $10^8$  reversals to failure.

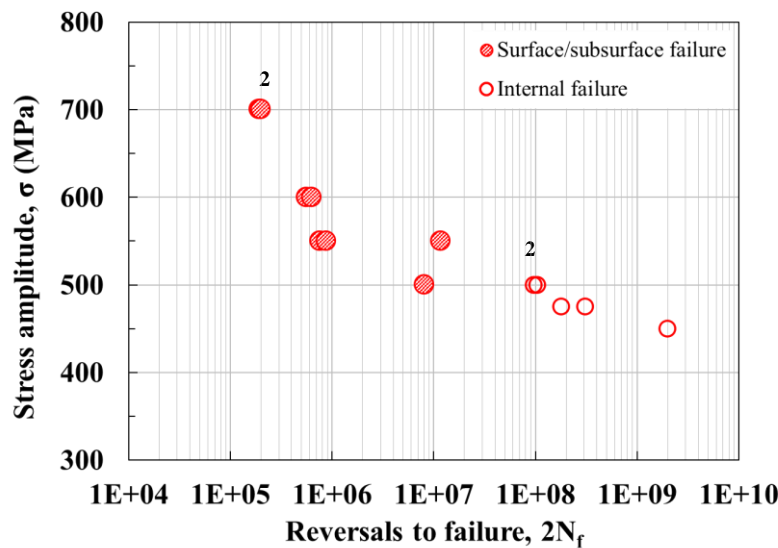


Figure 2. Ultrasonic fatigue-life data for L-PBF 17-4 PH SS specimens.

At lower stress levels, where fatigue failure originated from an internal defect, a fish eye area, which is a flat ring-like smooth region, are observed, as indicated in Figure 3. Inside the fish eye, there is a bright fine-grained area (fine granular topographic structure) around the crack initiating defect, which is also referred to as an optically dark area (ODA) or a fine granular area (FGA) [20,24,25]. The formation of ODA occurs around the internal defects in the VHCF regime, which has been attributed to the lower SIF of the cracks around the defect [15,20]. If the SIF of the cracks around the defects is higher than the threshold value, then ODA does not form neither the fish-eye [26]. ODA formation ends when the SIF reaches the threshold value for crack propagation inside the fish-eye area. For high-strength steels, Murakami et al. [27] attributed trapped hydrogen around the defects as the driver of microcrack nucleating from the defects [18] at lower stress levels, which continues up to the circumference of ODA until the crack becomes self-propagable. Shiozawa et al. [28] reported the decohesion of small carbides in the vicinity of defects/inclusions leading to the formation of small cracks, which coalesce with each other inside the ODA.

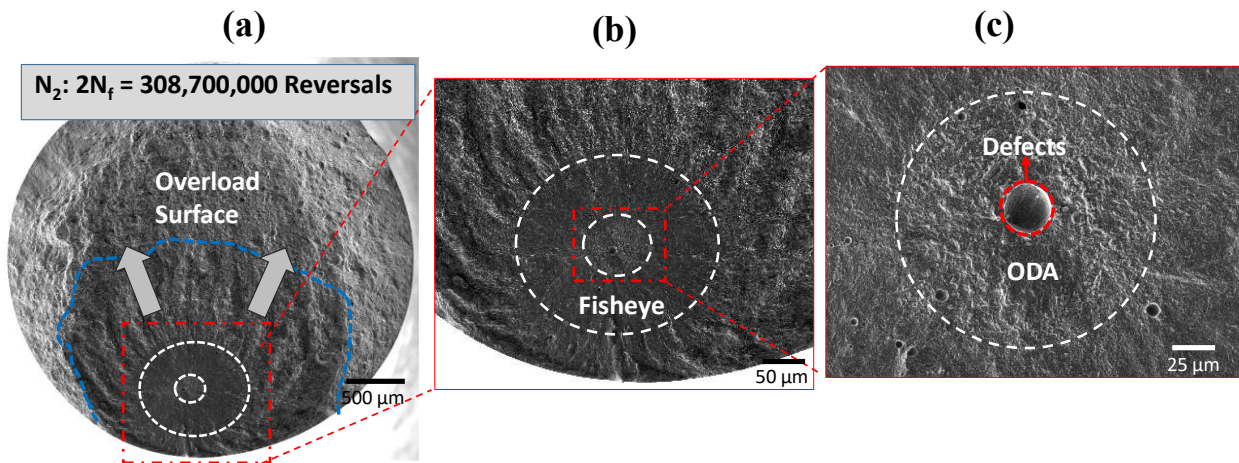


Figure 3. (a) Fatigue fracture surfaces of L-PBF 17-4 PH SS specimens tested at 475 MPa with 308,700,000 reversals to failure, (b) magnification of the fisheye, and (c) magnification of the ODA.

The location of the crack initiating defects was plotted against the stress amplitude, as displayed in Figure 4. It can be observed that as the stress level decreases, the crack initiates further away from the surface of the specimen towards the center. The transition from surface/subsurface crack initiation (less than 10  $\mu\text{m}$  from the surface) to internal crack initiation (up to 1,300  $\mu\text{m}$  from the surface) occurs at approximately 500 MPa.

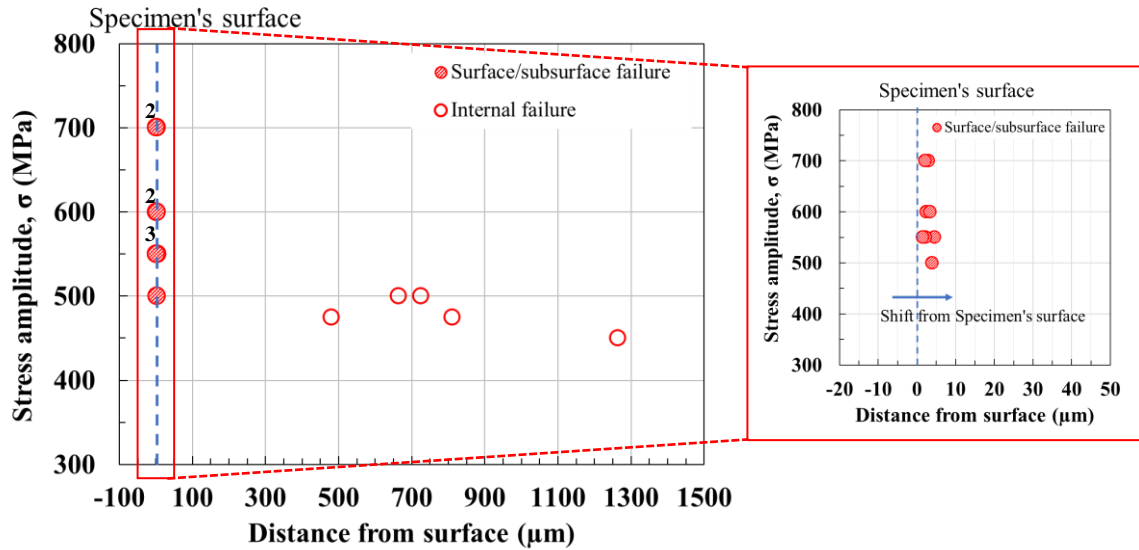


Figure 4. Stress amplitude against the distance of the crack initiating defects from the surface for L-PBF 17-4 PH SS specimens.

Figure 5 displays the representative size of the crack initiating pores,  $\sqrt{area}$ , against reversals to failure for all L-PBF 17-4 PH SS specimens. It can be observed in Figure 5a that for both internal and surface/subsurface defects, the fatigue life increases with the reduction in defect size. The size of ODA, formed around the internal defects, increases with the decrease in defect size, which can be attributed to the lower SIF of the crack inside the ODA. The larger area of ODA could be attributed to the small internal defect size and the corresponding threshold SIF required for the crack to be self-propagable within the fish eye region of the fracture surface [20,26]. For the VHCF regime, Murakami [20] reported that the use of  $\sqrt{area}$  of defect may lead to non-conservative prediction for several high-strength steels, and suggested that  $\sqrt{area}$  of ODA can be used in place of the  $\sqrt{area}$  of defect in Eq. (3). Therefore, the  $\sqrt{area}$  of ODA for L-PBF 17-4 PH SS specimens with internal failure were also obtained in this study, as shown in Figure 5b.

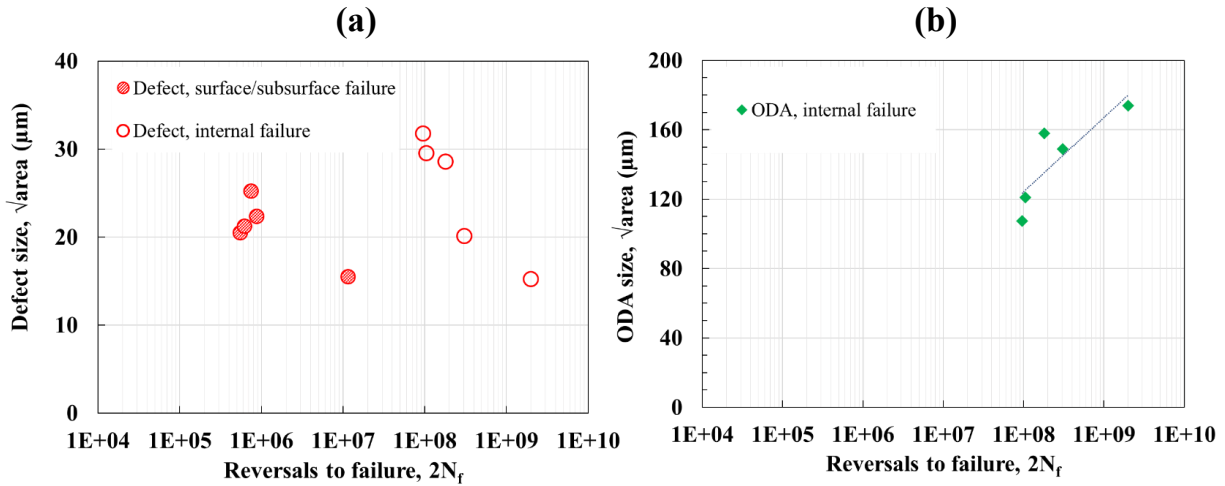


Figure 5. A representative size,  $\sqrt{area}$ , of defect or ODA against reversals to failure for L-PBF 17-4 PH SS specimens.

Using Eq. (4), the fatigue strength for L-PBF 17-4 PH SS specimens was obtained from either  $\sqrt{area}$  of crack initiating defect, or  $\sqrt{area}$  of the ODA surrounding the crack initiating defect. The analysis was performed for specimens whose lives are in the VHCF regime (i.e.,  $N_f > 10^7$ ). The comparison of the experimental and predictive fatigue strength with scatter bands of 5 and 10 is displayed in Figure 6. The experimental fatigue strength is the stress amplitude of individual fatigue testing. As can be seen, using  $\sqrt{area}$  of defect provides a better correlation between the experimental and predicted fatigue strength, with 67% of the data are within scatter bands of 10. Since the expression for parameter  $\beta$  in Eq. (4) was empirically determined from the data in Wang et al. [21] to include the dependency of fatigue life, the parameter  $\beta$  expression may need to be optimized based on the fatigue data in the current study for 17-4 PH SS. In addition, in Eq. (4), the Vickers hardness of 300 kgf/mm<sup>2</sup> was utilized for all analyses in this study. This hardness value was obtained at the surface of the L-PBF 17-4 PH SS specimen; however, the hardness may vary across the cross-section of the specimen, which would require further investigation [20].



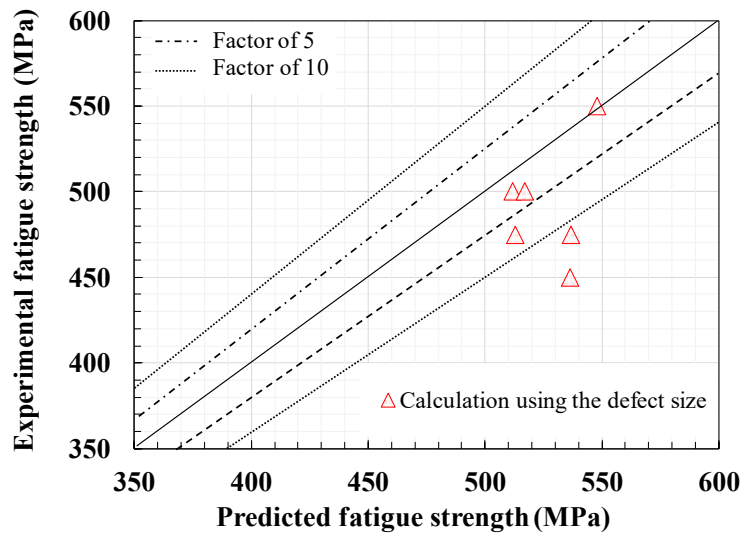


Figure 6. Predicted fatigue strength versus experimental fatigue strength in the VHCF regime with factors of 5 and 10 scatter bands for L-PBF 17-4 PH SS.

### Conclusions

In this study, the Murakami's  $\sqrt{area}$  approach was utilized to obtain the fatigue strength in the VHCF regime of L-PBF 17-4 PH SS. Ultrasonic fatigue tests were performed, and fractography analysis was conducted on all specimens to identify the crack initiating defects and failure region. The following conclusions can be drawn from this study:

1. The fatigue life of L-PBF 17-4 PH SS ultrasonic specimens spans from low cycle to beyond  $10^7$  reversals to failure, and the horizontal asymptote of the S-N curve to determine the classical fatigue limit was not observed.
2. All fatigue cracks initiated from gas entrapped pores in all the specimens. As the stress level lowered, the crack initiation sites shifted from the surface/subsurface region towards the internal region of the fracture surface. This transition occurred approximately at  $10^8$  reversals to failure.
3. For L-PBF 17-4 PH SS specimens with internal failure, the optically dark area (ODA) was observed surrounding the crack initiating pore. As the internal defect size becomes smaller, the size of ODA increases.
4. The modified Murakami's  $\sqrt{area}$  approach was adopted in this study to include the fatigue life dependency in the VHCF regime. The predictive fatigue strength using  $\sqrt{area}$  of defects correlated well to the experimental data for L-PBF 17-4 PH SS in this study.

### **Acknowledgment**

This paper is based upon the work partially funded by the National Institute of Standards and Technology (NIST) under Award No. 70NANB19H170. This paper describes objective technical results and analysis. Any subjective views or opinions that might be expressed in the paper do not necessarily represent the views of the NIST or the United States Government.

### **References**

- [1] Shamsaei N, Yadollahi A, Bian L, Thompson SM. An overview of Direct Laser Deposition for additive manufacturing; Part II: Mechanical behavior, process parameter optimization and control. *Addit Manuf* 2015;8:12–35. <https://doi.org/10.1016/J.ADDMA.2015.07.002>.
- [2] Soltani-Tehrani A, Yasin MS, Shao S, Shamsaei N. Effects of Stripe Width on the Porosity and Mechanical Performance of Additively Manufactured Ti-6Al-4V Parts 2021. <https://doi.org/10.26153/TSW/17627>.
- [3] Poudel A, Soltani-Tehrani A, Shao S, Shamsaei N. Effect of Powder Characteristics on Tensile Properties of Additively Manufactured 17-4 PH Stainless Steel 2021. <https://doi.org/10.26153/TSW/17610>.
- [4] Poudel A, Shamsaei N, Shao S. Linear Elastic Finite Element Calculations of Short Cracks Initiated from the Defects: Effect of Defect Shape and Size 2021. <https://doi.org/10.26153/TSW/17614>.
- [5] Stephens RI (Ralph I, Fuchs HO (Henry O. Metal fatigue in engineering 2001:472.
- [6] Effect of Hardness and Crack Shape on the Lower Critical Stress Intensity Factor Width  $\Delta K_{th}$  of Microcracks n.d. [https://www.jstage.jst.go.jp/article/jsms1963/35/395/35\\_395\\_911/\\_article/-char/ja/](https://www.jstage.jst.go.jp/article/jsms1963/35/395/35_395_911/_article/-char/ja/) (accessed July 29, 2022).
- [7] Singh R, Matsuo T, Hayashi K, Endo M. High-cycle fatigue strength prediction of ductile Ni-resist cast iron containing casting defects. *Int J Fatigue* 2022;163:107015. <https://doi.org/10.1016/J.IJFATIGUE.2022.107015>.
- [8] Schönbauer BM, Yanase K, Endo M. The influence of various types of small defects on the fatigue limit of precipitation-hardened 17-4PH stainless steel. *Theoretical and Applied Fracture Mechanics* 2017;87:35–49. <https://doi.org/10.1016/J.TAFMEC.2016.10.003>.
- [9] Schönbauer BM, Ghosh S, Kömi J, Frondelius T, Mayer H. Influence of small defects and nonmetallic inclusions on the high and very high cycle fatigue strength of an ultrahigh-strength steel. *Fatigue Fract Eng Mater Struct* 2021;44:2990–3007. <https://doi.org/10.1111/FFE.13534>.
- [10] Nezhadfar PD, Shrestha R, Phan N, Shamsaei N. Fatigue behavior of additively manufactured 17-4 PH stainless steel: Synergistic effects of surface roughness and heat

- treatment. Int J Fatigue 2019;124:188–204. <https://doi.org/10.1016/J.IJFATIGUE.2019.02.039>.
- [11] Romano S, Nezhadfar PD, Shamsaei N, Seifi M, Beretta S. High cycle fatigue behavior and life prediction for additively manufactured 17-4 PH stainless steel: Effect of sub-surface porosity and surface roughness. Theoretical and Applied Fracture Mechanics 2020;106. <https://doi.org/10.1016/j.tafmec.2020.102477>.
  - [12] Wu JH, Lin CK. Tensile and fatigue properties of 17-4 PH stainless steel at high temperatures. Metall Mater Trans A Phys Metall Mater Sci 2002;33:1715–24. <https://doi.org/10.1007/S11661-002-0180-8>.
  - [13] Nie D, Mutoh Y. Fatigue limit prediction of the matrix of 17-4PH stainless steel based on small crack mechanics. Journal of Pressure Vessel Technology, Transactions of the ASME 2013;135. <https://doi.org/10.1115/1.4023428/378305>.
  - [14] El Haddad MH, Topper TH, Smith KN. Prediction of non propagating cracks. Eng Fract Mech 1979;11:573–84. [https://doi.org/10.1016/0013-7944\(79\)90081-X](https://doi.org/10.1016/0013-7944(79)90081-X).
  - [15] Schönbauer BM, Yanase K, Endo M. VHCF properties and fatigue limit prediction of precipitation hardened 17-4PH stainless steel. Int J Fatigue 2016;88:205–16. <https://doi.org/10.1016/J.IJFATIGUE.2016.03.034>.
  - [16] ASTM A693-16. Standard specification for precipitation-hardening stainless and heat-resisting steel plate, sheet, and strip. ASTM International 2016;693:1189–97.
  - [17] Ultrasonic Fatigue Testing System | Shimadzu USF-2000A n.d.
  - [18] Yukitaka M, Masahiro E. Quantitative evaluation of fatigue strength of metals containing various small defects or cracks. Eng Fract Mech 1983;17:1–15. [https://doi.org/10.1016/0013-7944\(83\)90018-8](https://doi.org/10.1016/0013-7944(83)90018-8).
  - [19] Murakami Y, Endo M. Effects of defects, inclusions and inhomogeneities on fatigue strength. Int J Fatigue 1994;16:163–82. [https://doi.org/10.1016/0142-1123\(94\)90001-9](https://doi.org/10.1016/0142-1123(94)90001-9).
  - [20] Murakami Y. Metal fatigue: Effects of small defects and nonmetallic inclusions. Metal Fatigue: Effects of Small Defects and Nonmetallic Inclusions 2019:1–758. <https://doi.org/10.1016/C2016-0-05272-5>.
  - [21] Wang QY, Berard JY, Dubarre A, Baudry G, Rathery S, Bathias C. Gigacycle fatigue of ferrous alloys. Fatigue Fract Eng Mater Struct 1999;22:667–72. <https://doi.org/10.1046/J.1460-2695.1999.T01-1-00185.X>.
  - [22] Nezhadfar PD WJSJSSSN. High and very high cycle fatigue behavior of additively manufactured 17-4 PH stainless steel: Effect of shielding gas type 2022.
  - [23] Spriestersbach D, Brodyanski A, Lösch J, Kopnarski M, Kerscher E. Very high cycle fatigue of high-strength steels: Crack initiation by FGA formation investigated at artificial

- defects.                      Procedia                      Structural                      Integrity                      2016;2:1101–8.  
<https://doi.org/10.1016/J.PROSTR.2016.06.141>.
- [24] Sakai T, Nakagawa A, Oguma N, Nakamura Y, Ueno A, Kikuchi S, et al. A review on fatigue fracture modes of structural metallic materials in very high cycle regime. *Int J Fatigue* 2016;93:339–51. <https://doi.org/10.1016/J.IJFATIGUE.2016.05.029>.
- [25] Nakamura T, Oguma H, Shinohara Y. The effect of vacuum-like environment inside sub-surface fatigue crack on the formation of ODA fracture surface in high strength steel. *Procedia Eng* 2010;2:2121–9. <https://doi.org/10.1016/J.PROENG.2010.03.228>.
- [26] Spriestersbach D, Brodyanski A, Lösch J, Kopnarski M, Kerscher E. Very high cycle fatigue of high-strength steels: Crack initiation by FGA formation investigated at artificial defects.                      Procedia                      Structural                      Integrity                      2016;2:1101–8.  
<https://doi.org/10.1016/J.PROSTR.2016.06.141>.
- [27] Murakami Y, Nomoto T, Ueda T, Murakami Y. On the mechanism of fatigue failure in the superlong life regime ( $N > 10^7$  cycles). Part 1: influence of hydrogen trapped by inclusions. *Fatigue Fract Eng Mater Struct* 2000;23:893–902. <https://doi.org/10.1046/J.1460-2695.2000.00328.X>.
- [28] Shiozawa K, Lu L, Ishihara S. S–N curve characteristics and subsurface crack initiation behaviour in ultra-long life fatigue of a high carbon-chromium bearing steel. *Fatigue Fract Eng Mater Struct* 2001;24:781–90. <https://doi.org/10.1046/J.1460-2695.2001.00459.X>.